

Multiple stages of smoking phenomenon in electron beam powder bed fusion process

Dongfang Wang^{a,b}, Dechen Zhao^{a,b}, Xiaoyu Liang^{a,b,*}, Xiang Li^{a,b}, Feng Lin^{a,b,*}

^a Department of Mechanical Engineering, Tsinghua University, Beijing, China

^b Key Laboratory for Advanced Materials Processing Technology, Ministry of Education of China, China

ARTICLE INFO

Keywords:

Electron beam powder bed fusion
Smoking
Powder
Electronic signal monitoring
Simulation

ABSTRACT

Smoking is a unique phenomenon in the electron beam powder bed fusion (EB-PBF) process. The far-field effect and fast expansion features of smoking often cause the destruction of the powder bed, resulting in part failure or even equipment damage, which seriously restricts the application and development of EB-PBF. However, the generation and development of the “powder cloud” during the smoking process are yet open research questions. This study proposed and established optical & electronic monitoring systems to observe the process of smoking and collect electronic signals to reveal the mechanism behind smoking. Simulation at a small scale where the powder motion of each powder at the affected zone in the powder bed is described by the discrete element method was conducted to simulate the effect of the inertial force and electrostatic force. Observations demonstrated that the smoking process consists of multiple stages. The powder bed showed different motion characteristics and generated different electronic signal patterns at different stages. Numerical simulations revealed that the electrostatic force is the main driving force and confirmed the promoting effect of charged particles striking the powder bed on smoking expansion. The current study provided interpretations of the mechanism as well as a potential solution for real-time monitoring and smoking prevention.

1. Introduction

Electron Beam Powder Bed Fusion (EB-PBF) technology forms three-dimensional entities layer by layer using an electron beam to melt and solidify metal powders in a specified area for each layer [1–3]. Compared to the laser powder bed fusion process, the EB-PBF process can offer a high preheating temperature due to the high energy efficiency of electron beam, which provides advantages for intermetallic, non-weldable superalloys and refractory metals [4]. However, the transient interaction between the electron beam and long can cause a violent powder movement, known as “smoking” [5,6]. Smoking is a unique phenomenon during the EB-PBF process, which occurs in the interaction area between the electron beam and the powders and then rapidly expands outward on an explosive type. During smoking, powders on the building platform are lifted and scattered into the vacuum chamber, destroying the powder bed, and the EB-PBF process is terminated irreversibly. The presence of smoking may cause fabrication failure or even equipment damage, which seriously restricts the application and development of EB-PBF.

Smoking is conventionally prevented by obtaining the non-smoking

process parameter window through numerous trial and error experiments [7,8]. Besides, preheating is one of the most effective methods to prevent smoking, which is aimed at slightly sintering powder particles together to improve the mechanical strength of the powder bed [9–11]. With the help of preheating, many materials can be prepared by EB-PBF now. However, the introduction of the preheating process into EB-PBF does not inhibit smoking completely. The search for a solution to prevent smoking is continuing. Wayland Ltd. adopted a “neutral beam” technology to reduce the charge input into powders with the same beam current, in order to reduce the probability of smoking [12]. Joel Ltd. proposed to use the “e-shield” device to suppress smoking [13]. The two above specific technologies claimed to solve the smoking issue without providing detailed explanations of the operating principles. In addition, Arcam AB. used an X-ray sensor installed on the side wall of the electron gun to monitor for splashed powder inside the electron gun. This method was expected to prevent the electron gun from damage, but the sensor did not respond until the powders completely expanded [14].

It is difficult to observe the smoking process because it develops rapidly. With optical observation experiments, existing research can capture images of the smoking phenomenon, indicating smoking occurs

* Corresponding authors at: Department of Mechanical Engineering, Tsinghua University, Beijing, China

E-mail addresses: xiaoyu.liang@tsinghua.edu.cn (X. Liang), linfeng@tsinghua.edu.cn (F. Lin).

<https://doi.org/10.1016/j.addma.2023.103434>

Received 26 October 2022; Received in revised form 7 January 2023; Accepted 27 January 2023

Available online 1 February 2023

2214-8604/© 2023 Published by Elsevier B.V.

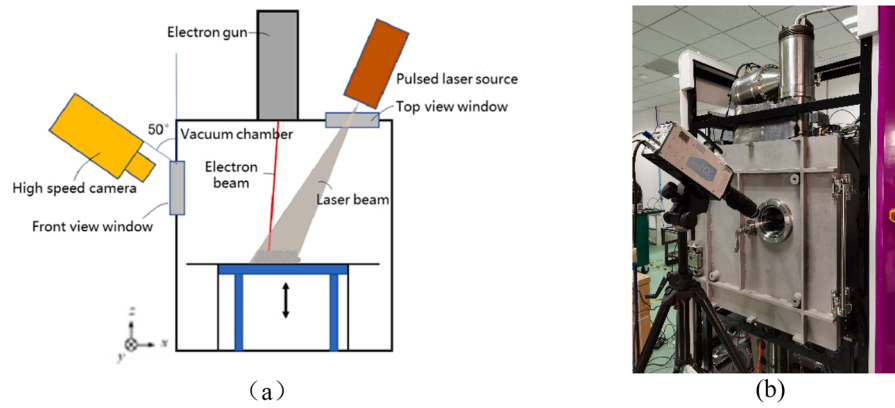


Fig. 1. High-speed photographic image system: (a) schematic illustration; (b) exhibition of equipment.

in the form of an explosion [15,16]. The mentioned references suggested that the start of smoking originates from powder charging. However, the main driving force of smoking is controversial until now, especially considering unique characteristics like the “far-field effect”. Different explanations for the smoking mechanism were given. Qi et al. [17] suggested the impact force (F_e) from electron momentum is the main cause of smoking. Considering the far-field effect of smoking, Kahnert et al. [18] indicated that smoking results from Lorentz force (F_L) from the magnetic field created by the electron beam. Sigl and Milberg [15, 19] suggested three main driving forces: recoil force (F_g) caused by evaporation of residual water on powder surface, impact force, and electrostatic repulsive force (F_q) caused by powder charge accumulation. Zhou et al. [20] eliminated the possibility of F_e and F_g as the main driving forces through controlled trials. Eschey et al. [16] proposed the equivalent circuit model of the whole powder bed and listed the calculation formulas of F_e , F_L , F_q . Cordero et al. [21] proposed a circuit model to calculate the charge dissipation of powders in a single row, confirming that F_q is of sufficient magnitude to cause smoking. Chiba et al. [22,23] measured the direct current (DC) resistivity and alternating current (AC) impedance of the powder bed, obtaining a reliable value for the equivalent circuit.

However, there is still not a comprehensive explanation for the smoking start and development mechanism, especially the mechanism for the far-field effect and rapid expansion, which contributes greatly to the rapid destruction of the powder bed [24]. So far, reports of observations on the process of smoking were limited in the literature. In addition, existing research models only approximately calculate the magnitude of forces acting on static powders [21,25,26]. Simulations

taking into account the particle movement and the arrangement of powders on the powder bed were deficient.

The objective of this work is to observe powder movement during the process of smoking and investigate the mechanisms of the different smoking stages. In this work, a self-built Electron & Optical Observation system is used to realize multi-scale observation through optical high-speed photography and electronic signal detection. Based on this system, a real-time monitoring method for smoking is proposed. Moreover, a discrete element model (DEM) involving charge dissipation is developed to help investigate the characteristic phenomena during smoking.

2. Apparatus set-up and experimental campaign

2.1. Optical observation system and electronic detection system

To achieve direct observation and responsive detection of the smoking phenomenon during the EB-PBF process, a high-speed imaging system and an electronic signal detecting and processing system have been established respectively in the framework of this research project. The two systems serve as auxiliary modules of the EB-PBF machine QbeamLab 200 from QuickBeam Tech. Co, Ltd.(Tianjin, China).

The high-speed imaging system depicted in Fig. 1 includes a high-speed camera, a pulsed laser light source, a fixed focus lens, and a band-pass filter. The camera used was a NAC MEMRECAM HX-6 with a maximum frame rate of 210k Frames/s. The pulsed laser light source was CAVILUX HF with a central wavelength of 808 nm and maximum output power of 500 W. The laser light source was triggered synchronously with the high-speed camera through the CAVILUX control unit to ensure sufficient illumination intensity during high-speed imaging. The

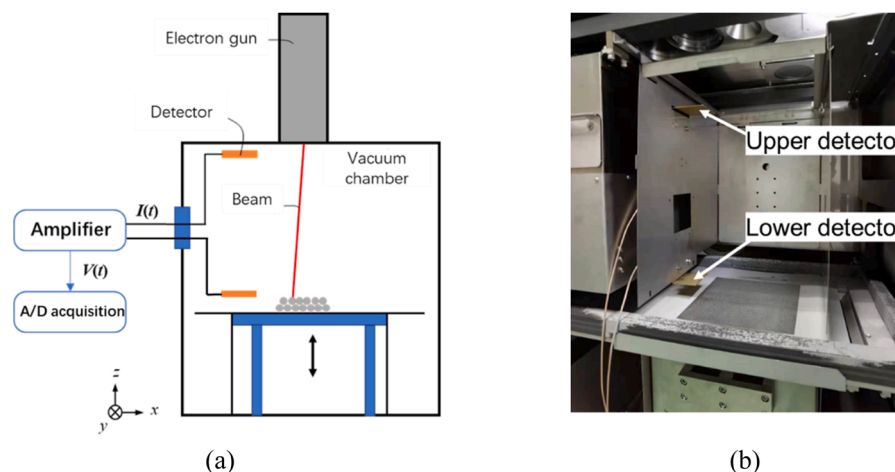


Fig. 2. Electronic signal detection system: (a) schematic illustration; (b) exhibition of the equipment.

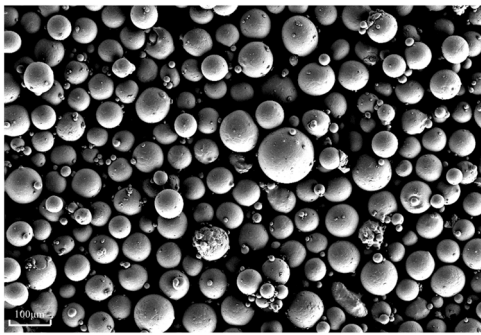


Fig. 3. Micromorphology of gas-atomized Ti6Al4V powder.

high-speed camera was placed in front of the observation window at an angle of 50° from the vertical. The distance between the observation window and the center of the building platform was about 300 mm. A fixed focus lens with a focal length of 200 mm (Nikon ED AF MICRO NIKKOR 200 mm 1:4D) was selected to obtain a good field of view and clear powder shape. To prevent (1) the influence of other visible light sources, (2) electron gun cathode glow, and (3) visible light caused by electron beam powder interaction, a band-pass filter with a central wavelength of 808 nm and a bandwidth of 10 nm was installed in front of the lens.

The electronic detection system is depicted in Fig. 2. The system consisted of two detection plates, an I/V converting amplifier, and an accurate A/D acquisition card based on the design proposed in [27]. Two metal detection plates made of H62 copper alloy were arranged at the top and bottom of the vacuum chamber respectively, and the detection surfaces were parallel to the X-Y plane of the forming coordinate system. The vertical height of the lower detection plate from the building platform was about 20 mm which was very close to the powder bed. The aforementioned detectors' arrangement was picked mainly to capture electrons or charged powder from different directions. The upper detection plate can capture radiated electrons generated by the action of electron beam material and charged powder particles splashed during smoking. The lower detection plate mainly receives the charged powder during smoking.

Current signals from detection plates were led out from the vacuum chamber through the coaxial signal line, connected to the I/V converting amplifier. These weak current signals were converted into a voltage signal of -5 – 5 V by an amplifier and gathered by an A/D acquisition card. Considering the complexity of the electromagnetic environment of the vacuum chamber, the I/V converting amplifying circuit was designed to be a precision operational amplifier circuit with low noise. As shown in Fig. 2(a) in the circuit diagram, the gain of the amplifier is 100 KV/A, and the maximum output voltage is 5 V. Therefore, the measuring range of the detection system is 50 μ A.

A PCI8514B A/D acquisition card from ART Ltd. was utilized, the sampling frequency of the electronic detection system was set to 1 MHz to quickly record the electronic signal in the smoking process, and the signal acquisition was triggered by the rising edge signal of QbeamLab control software.

2.2. Method to trigger smoking via EB-PBF system

With the design and installation of the observation equipment, the method to trigger smoking via the EB-PBF system was conducted to characterize the powder behavior. To characterize powder behavior, smoking was triggered on the QbeamLab 200 EB-PBF machine. Ti6Al4V was used as the powder material because it is a common EB-PBF material and is prone to smoking. Observation under a scanning electron microscope is shown in Fig. 3. The particle size distribution was 45–105 μ m with an average diameter of 75 μ m. The feeding density is 2.58 g/cm³, and the Hall flow rate is 23 s/50 g. The chemical

Table 1
Alloying composition of gas-atomized Ti6Al4V determined via ICP.

Element	Ti	Al	V	C	Fe	O	N
at%	residue	4.01	6.28	0.018	0.029	0.06	0.01

Table 2
Parameters in the electron beam scanning experiments.

ExperimentParameters	Fixed-point irradiation	Single-line repeated scanning	Multi-line scanning
Layer thickness (mm)	0.5	0.5	0.5
Irradiation duration (s)	0.5	/	/
Beam current (mA)	2	2	2
Accelerating voltage (kV)	60	60	60
Scanning speed (m/s)	/	4	4
Scanline length (mm)	/	60	60
Line offset (mm)	/	/	5
Chamber pressure (Pa)	0.15	0.15	0.15

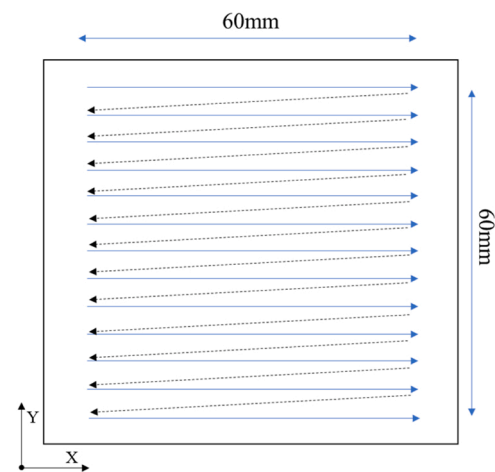


Fig. 4. Illustration of the multi-tracks scanning strategy.

composition is shown in Table 1.

The optical observation experiment of smoking includes fixed-position irradiation and single-line repeated scanning. To ensure that the smoking phenomenon can be triggered, the preheating process is intentionally omitted. This experimental design differs slightly from the actual production, but can better demonstrate the characteristic behavior of the powder bed under the action of the electron beam. The experimental parameters of fixed-position irradiation are shown in Table 2. First, Ti6Al4V powders with a thickness of 0.5 mm were spread on the substrate and then irradiated with a 1 mA current beam. The powder bed was irradiated at a fixed point by a focused electron beam with a beam current of 2 mA for 0.5 s to trigger the smoking phenomenon and recorded by the high-speed camera. The electron detection experiment of smoking includes fixed-position irradiation and multi-line scanning. The electron detection experiment at a fixed point was carried out simultaneously with the optical observation experiment, i.e., as shown in Table 2. In the multi-line scanning experiment, a 2 mA focused electron beam was used to scan the powder bed at the speed of 4 m/s. Raster scanning mode was utilized, and the scanning pattern is shown in Fig. 4. Solid arrow indicates the scanning line, while the dashed arrow indicates the skip track between each scanning line. In the experiment, the electronic detection system continuously collects electronic signals from the detection plates.

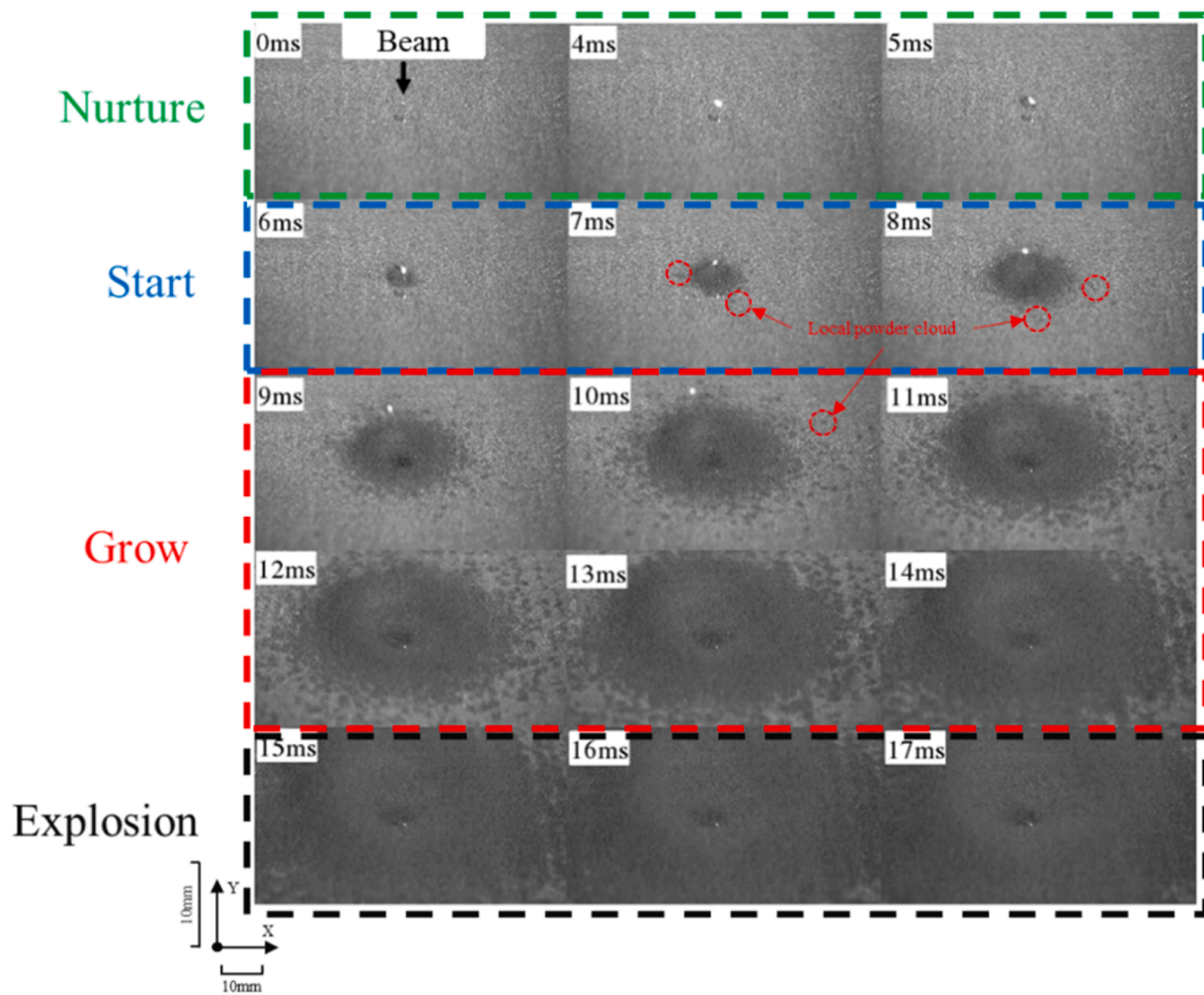


Fig. 5. High-speed photographic image of smoking development process under the condition of fixed-position irradiation (Movie 1, in Supporting information).

3. Results of optical observation and signal measurement

3.1. High-speed photographic image

3.1.1. Irradiation at a fixed position

Fig. 5 and Movie 1 (in Supporting information) show the smoking process when the powder bed was irradiated by an electron beam with a current of 2 mA at a fixed position, captured by the high-speed camera. A large dark spot above the irradiated position has been seen which was called the “powder cloud” by Kahnert et al. [18]. The powder cloud hindered the diffuse reflection from the illumination light source on the powder bed below them. Similarly, the small powder disturbance on the powder bed weakened the diffuse reflection effect and appeared as dark spots. With the help of this special brightness and darkness feature, some characteristics of powder movement during smoking can be recognized and tracked macroscopically, according to which smoking can be divided into different stages.

The first 5 ms was the “nurture stage” of the smoking phenomenon. During this period, under electron beam irradiation, the powders remained in the powder bed. At 4 ms, there was an obvious bright spot due to high-temperature radiation, which means powders in the irradiated area might be sintered. The electron beam charged the powder bed resulting F_q increased gradually as micro-sintering occurred between powders. The micro-sintering hindered the free motion of powders, increasing the overall stiffness of the powder bed. There was a competitive relationship between the rising F_q and rising stiffness of the powder bed, which determined whether the smoking continues.

Following the “nature stage” is the “start stage” of the smoking process. During this period, charged powders began to leave the powder bed and substrate. There was a powder cloud generated above the irradiated area and vanished repeatedly. At 5 ms, a local dark spot appeared on the left side of the concerned area, indicating that the powder bed became loose, and a small amount of powder left the powder bed and formed a small powder cloud above it. During 6–8 ms, the dark spot expanded continuously, indicating that the powder cloud continuously expanded outward with the irradiated position as the center.

The following stage up to 14 ms is the “grow stage” of smoking. During this period, the “powder cloud” continued to expand, meanwhile, an increasing number of powder clouds appeared around the concerned area. Compared to the powder cloud that occurred during the “start stage”, the newly generated “powder clouds” are much smaller, looking like dense “craters”. With the emergence of craters, the range and severity of smoking increased sharply, similar to the “chain reaction” mode, and the smoking process became irreversible. At 9 ms, many discrete small powder clouds were observed on the periphery of the central powder cloud. In this process, the moving powders transferred momentum to the static powders through collision and transferred charge through short contact. After the strike, the static powders obtained initial velocities, caused by momentum transfer, and accelerations, caused by forces from charge accumulation. At one of the impact areas, part of the impacted powders rose above their initial position and formed a powder cloud, also called “local powder cloud” according to its location; The other part splashed towards their peripheral area and

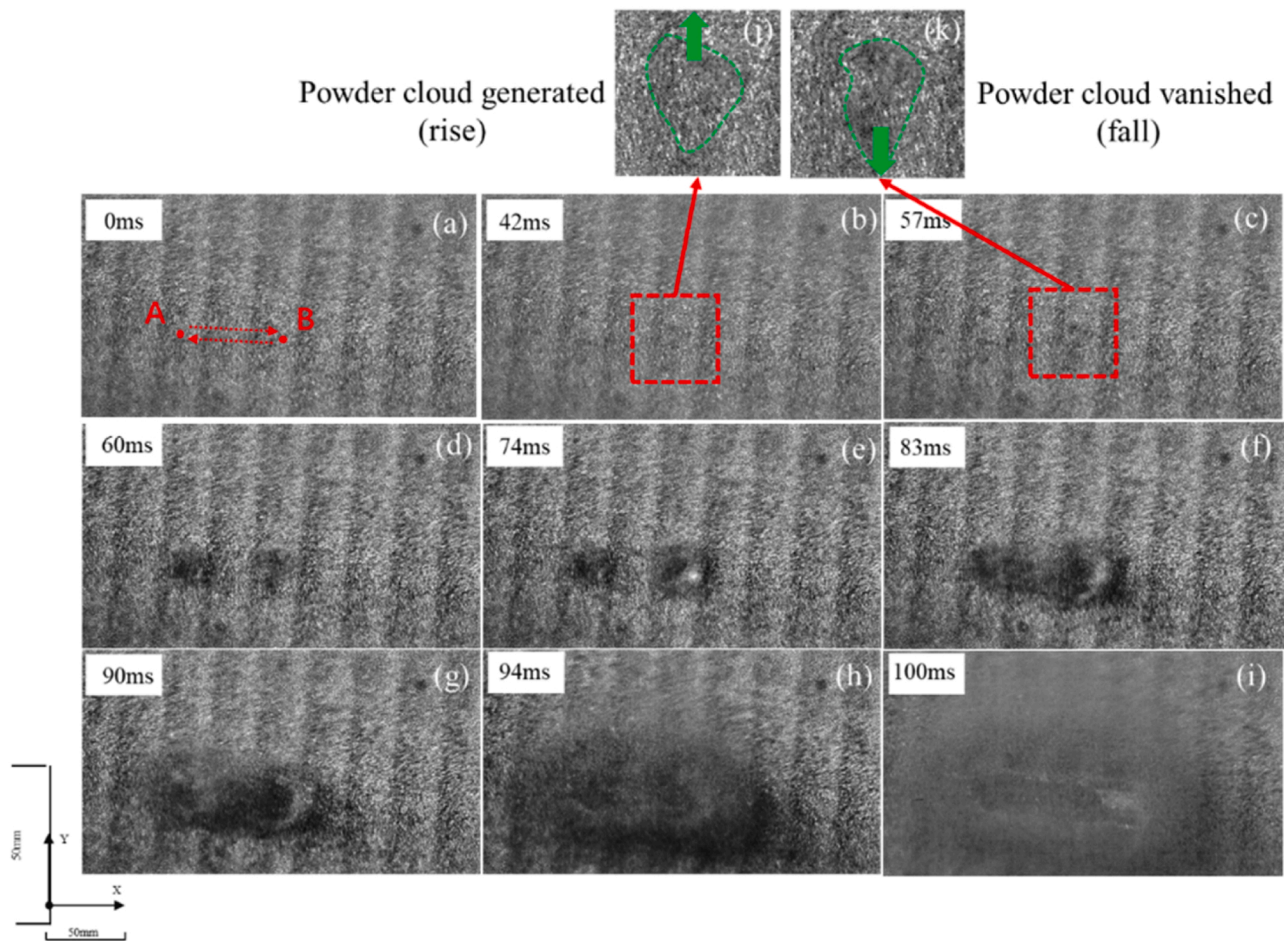


Fig. 6. High-speed photographic image of the smoking development process under the condition of single-line repeated scanning. Points A&B in (a) were endpoints of the scanline; (j)(k) are the enlarged views of (b)(c); the green curve in (j)(k) is the local powder cloud, and the green arrows indicate the moving directions. (Movie 2, in Supporting information).

caused more secondary impacts. After this process, there was a loss of powders in every impacted area and the substrate was exposed. These areas are called “craters”. Fig. 8(f)–(i) are the schematic illustrations of the crater generating and expanding process, Fig. 8(j) shows the moving track of splashed powder from the central area (powder A) and struck powder from a crater (powder B). As described, splashed powders from one crater might lead to one or even more secondary craters. The number of craters increases with the speed of the “chain reaction”. At the same time, the central powder cloud continued to expand outward and gradually “devoured” small local powder clouds, as shown in Fig. 8(d), expanding the range of smoking rapidly. The formation of craters may be the main mechanism of the rapid expansion of smoking.

After 14 ms was the “explosion stage”. During this period, smoking was fully developed, as shown in Fig. 8(e). Some of the powders flew smoothly and disorderly and impacted the substrate repeatedly, while others finally fell under the action of gravity.

3.1.2. Single-line repeated scanning

During production, the electron beam moves along the scanning lines and melts the powder bed. In the previous section, we obtained high-speed photographic images of powder behavior under fixed-point irradiation. To investigate the specific smoking process during production, images of powder behavior during single-line repeated scanning were obtained by the same optical observation system.

Fig. 6 and Movie 2 (in Supporting information) show the smoking process during single-line repeated scanning with a 2 mA electron beam moving at 4 m/s. Each back-forth scanning track of the electron beam is

defined as one cycle (as shown in Fig. 6(a) with points A and B representing the start and end of a scanline). As scanning started, powders near the irradiation point moved. The horizontal movement was much larger than the vertical component, which means powders were rearranged only on the surface of the powder bed while no powder cloud formed. After about 42 ms, when the beam spot reached point B in the second cycle, a local powder cloud formed at point B but immediately vanished as the beam spot moved away. When the beam spot reached points A and B at 60 ms and 74 ms, two larger powder clouds formed. After that, two powder clouds continuously expanded and then combined into a “central powder cloud” with a larger size. The “central powder cloud” expanded with a higher speed and the whole powder bed was raised finally.

Supplementary material related to this article can be found online at [doi:10.1016/j.addma.2023.103434](https://doi.org/10.1016/j.addma.2023.103434).

It took about 100 ms from the start of scanning for the smoking process to finish. The single-line repeated scanning smoking process lasted about 8 times as long as the fixed-point irradiation experiment. This was because as the beam spot moves, the average irradiation time of each powder is much less than the total experiment duration, which means the average charging rate is lower than that in the fixed-point irradiation experiment.

It was noted that there was a small local powder cloud appearing for a short time and then quickly vanishing before the explosion. When the irradiated area was about to enter the “explosion” stage and produced a local powder cloud with continuous charge accumulation, the beam quickly moved away and there was not enough charge input to maintain

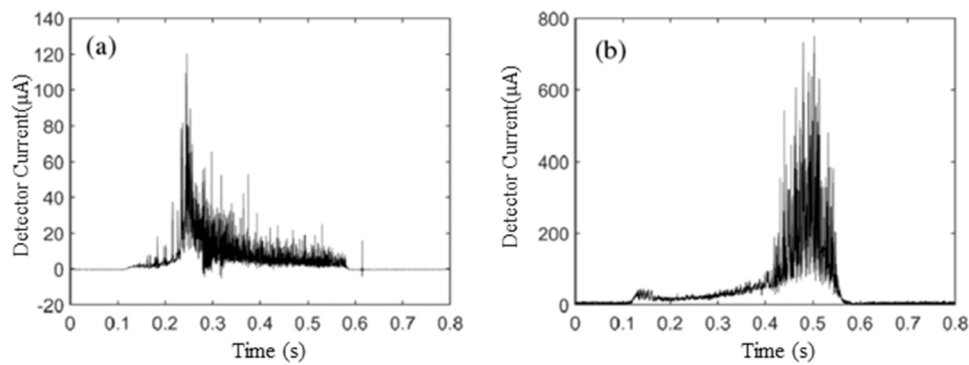


Fig. 7. Signals of fixed-position irradiation, (a)upper detector, (b)lower detector.

the development of the powder cloud. When the beam irradiated the area again where the powder cloud was once generated, the charge accumulated again quickly until it was enough to maintain the development of smoking. Then the vanishing local powder cloud was “activated” and continued to expand.

In each half cycle, each powder was irradiated for the same duration of time and was irradiated twice in a whole cycle. However, the interval time between irradiations is different for the powders at different positions, which results in the spatial inhomogeneity of powder charge-discharge characteristics in a cycle. The interval time of powders at line endpoints was the shortest. And we found that the local powder clouds tended to appear at the end of the scanline. This finding agreed with the charge-discharge theory proposed by Cordero et al. [21].

The results revealed that smoking is a sequential rather than transient process, which requires continuous and sufficient charge input to maintain. The repeated charge-discharge process resulted in a repeated generation-vanishing process of the local powder cloud and a delay time between the local powder cloud generation and final smoking, which can be controlled by modifying the process parameters. It can be inferred that under the same beam power smoking can be inhibited or avoided by adjusting the scanning parameters including scanning speed, beam size, and scan path. On the other hand, if the local powder cloud can be identified as a powder abnormal state, the interval time between local powder cloud generation and smoking occurrence makes real-time smoking monitoring and identification feasible.

3.2. Electronic signals Analyses

3.2.1. Electronic signal of irradiation at a fixed point

In the experiment of irradiation at a fixed position, the upper and lower detectors simultaneously recorded the electronic signals during smoking. Electronic signal characteristics mainly included base value, pulse disturbance, noise signal, etc. The noise signal mainly came from the inherent noise of the beam power supply; The base value represented the number of electrons reaching the detectors in unit time. The signal acquisition was triggered when capturing a rising-edge signal from the control software of the EB-PBF device. The delay might be attributed to the accumulated effects of signal filtering, response of acquisition software, in particular, the device response. It indicated the start of irradiation when obvious signal increasing was detected.

Fig. 7(a) shows the electronic signal from the upper detector. At 0.1 s, the electron beam began irradiating, and the backscattered electrons and secondary electrons were generated and moved to the vacuum chamber, partly captured by detectors. The base value of the electronic signal rose at that time, but then quickly both two detectors appeared to pulse disturbances. The upper detector responded faster, but the overall peak value is small. At 0.15 s, many pulses with low peak values of 5–20 µA appeared, and the base value rose slightly; At 0.25 s, pulses with large peak values of 50–120 µA appeared, and the base value rose rapidly. After 0.25 s, the pulse peak values decreased along with a sharp

attenuation of the base value. At 0.6 s, the beam was turned off and the signal appeared stable. As shown in Fig. 7(b) is the signal from the lower detector. At 0.1 s, there are many pulses with a low peak value of 5–30 µA. During 0.1–0.2 s, the pulse peak values the base value decreased slowly; During 0.2–0.42 s, the pulse peak values the base value rose slowly; During 0.42–0.53 s, the pulses with large peak values of 150–600 µA appeared, along with the increase of base value. After 0.53 s, the signal decays rapidly. The beam is turned off after 0.6 s, and the signal becomes stable.

The occurrence time and peak values of pulse reflected the powder movement and electrical characteristics during smoking at the macro-scale. According to optical observation results, smoking lasted about only 20 ms from the nurture to the explosion stage. Meanwhile, the disturbances of electronic signals from each detector lasted 500 ms, the biggest signal change appeared 100 ms and 300 ms later than the irradiation start respectively on the upper and lower detectors. These pulse disturbances resulted from spattered powders intermittently striking the detectors. As Fig. 7 shows, the pulse disturbances on the lower detector appeared 200 ms later than the upper detector. As smoking developed, some spattered powders with large amounts of charge rose and fell, finally struck the lower detector under the action of gravity. As result, pulses with high peak value appeared on the signal of lower detector, as shown in Fig. 7(b).

Another thing worth noting was that the signal base value from the lower detector first decreased and then increased before obvious pulse disturbances appeared. The change in base value resulted from the influence of powder behaviors on electron spatial distribution in the vacuum chamber. The interaction between the electron and powder cloud influenced the trajectory of electrons. The continuous impacts between powder and electron could change the electron moving direction. As a result, the electron beam was scattered after passing through the powder cloud, as shown in Fig. 8(b)–(e). On the other hand, the impacts could also result in secondary electrons or backscattered electrons emission from the irradiated area. The “mixed” electrons consisted of secondary electrons and backscattered electrons emitted to the vacuum chamber and were partly captured by detectors, as shown in Fig. 8(a)–(e). After entering the explosion stage, the electron beam scattered after electrons impacting with powders on their tracks. Fewer secondary and backscattered electrons could reach the lower detector, resulting in a decrease in the signal base value, as has been revealed in the work of Yim et al. that the penetration depth of the electron beam on the powder bed is limited [28]. After 0.25 s, when most of powders began to fall due to gravity, the size of the powder cloud gradually decreased, resulting in the attenuation of electron beam scattering and an increase of signal base value. Meanwhile, the base value of the upper detector rose continuously after smoking happened. This was because as powder constantly splashed into the vacuum chamber, the position of mixed electrons emission point became higher. The response of the electronic signal to the presence of a powder cloud appears to be faster than the powder-detector striking. It could be possible to predict or even prevent

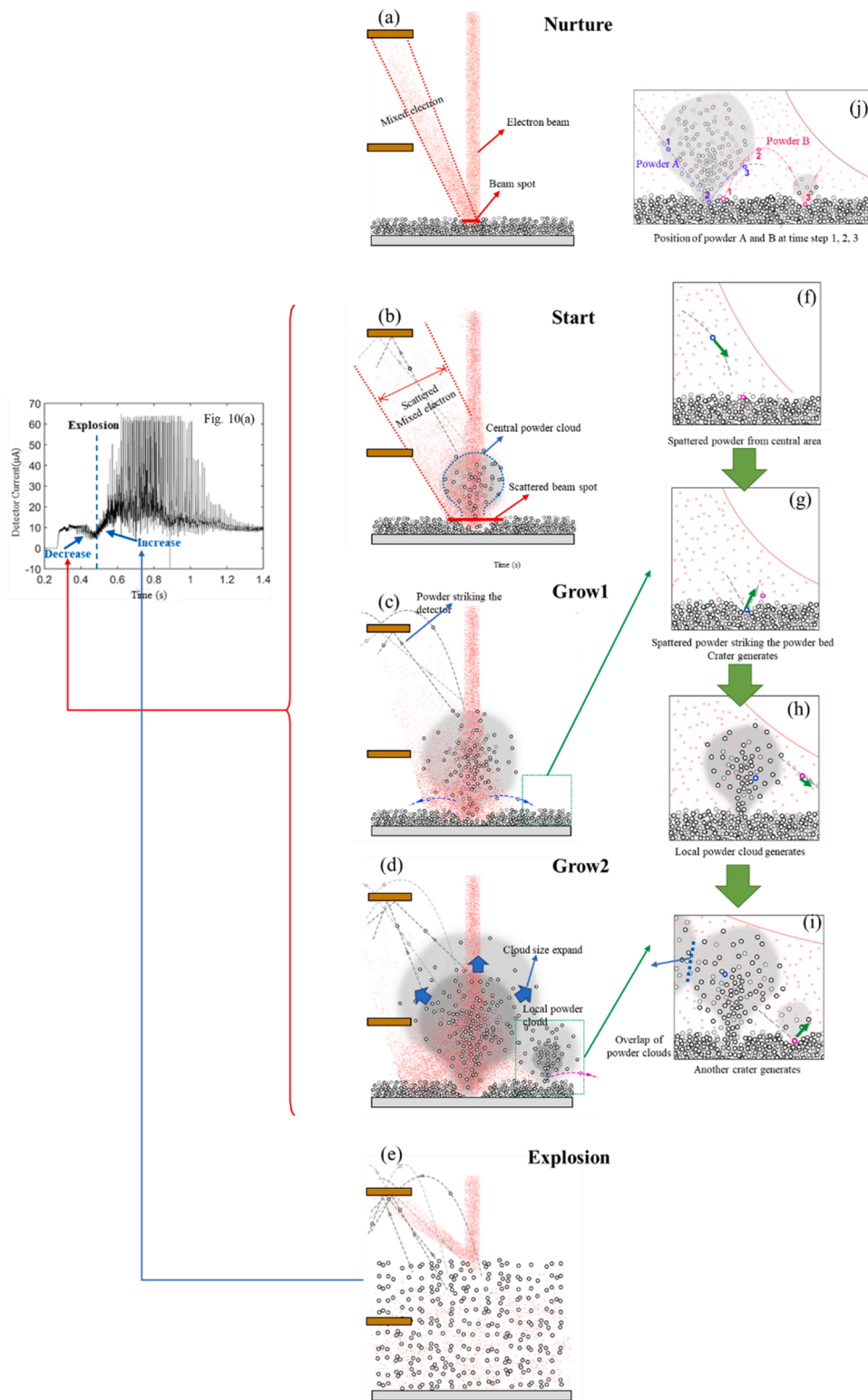


Fig. 8. Schematic illustration of powder movement during smoking process. The red punctate zone is electrons, the grey area is powder cloud, the dashed grey lines are moving tracks of splashed powders. (a) Nurture stage; (b) Start stage: central powder cloud generated, mixed electrons were scattered. The dashed arrow is the moving track of splashed powders towards the upper detector; (c)-(d) Grow stage: powder cloud size expanded, craters generated and expanded to the surrounding area, local powder cloud generated and overlapped with central powder cloud; (e) Explosion stage: powders splashed to the whole chamber, the electron beam was scattered while mixed electrons consist of backscattered and secondary electrons emitted to the upper detector on the upper surface of huge powder cloud; (f)-(i) Generation and expansion process of craters; (j) Moving tracks of interested powder A and B. The wide blue arrow in (d) stands for expanding direction of the powder cloud, the dashed grey lines with arrows in (b)-(i) are the moving tracks of several splashed powders.

smoking by monitoring the signal of powder cloud as a warning signal.

The total charge received by the detector in the pulse time can be obtained by integrating a single pulse in the time domain. Fig. 9 shows the enlarged view of the signal curve, selecting six typical pulses and calculating the charge amount respectively. It can be found that the charge received by the detector in a single pulse time was $10^{-8} - 10^{-7}$ C, indicating the charge of the corresponding powders. These data also provided an important reference for the subsequent simulation study of

the smoking mechanism.

In general, the electronic monitoring system can characterize the spatial distribution of powders in the vacuum chamber at the macro-scale. The corresponding typical signal characteristics responded to the powder motion state in different stages of smoking. Theoretically, by identifying these signal characteristics, we can judge whether smoking occurs and at which stage, and then take measures to stop the further development of smoking. However, in the case of fixed-position

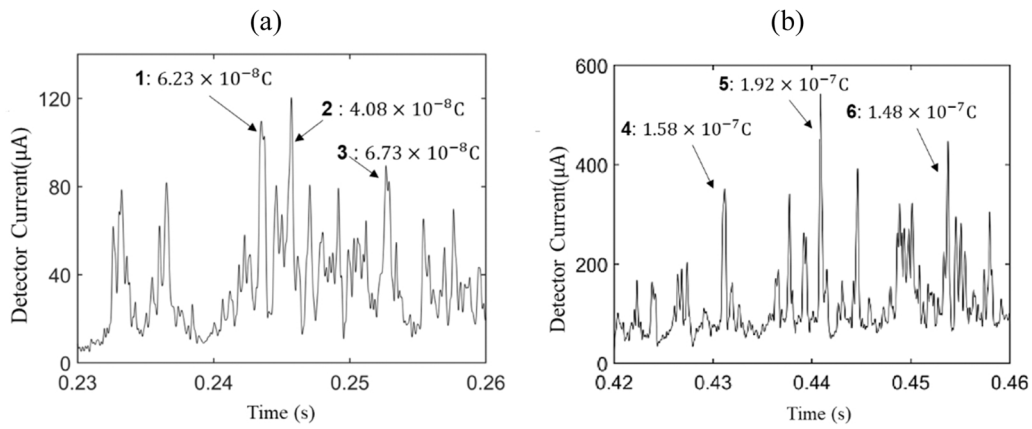


Fig. 9. Pulse disturbance of signals and corresponding charge amount, (a)upper detection plate, (b)lower detection plate.

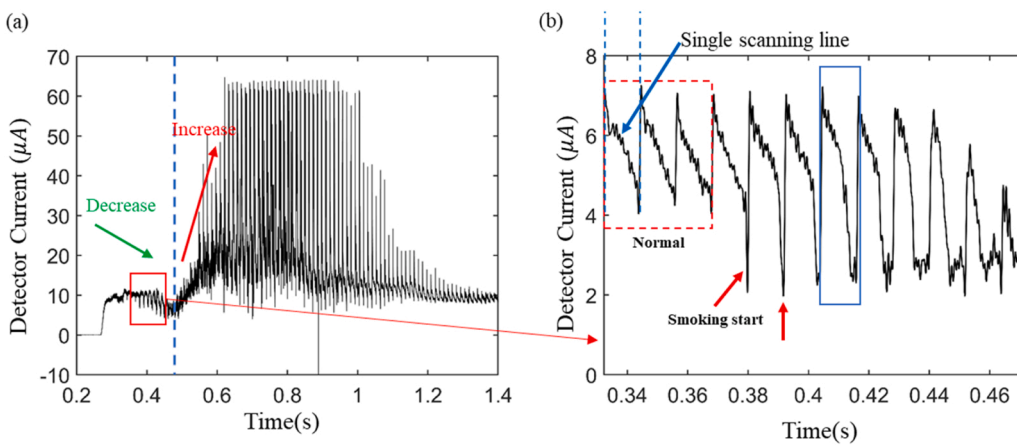


Fig. 10. Characteristic signal of smoking during EB-PBF process (b)is an enlarged view of the red box area in (a).

irradiation, smoking occurs very quickly (only last 10 ms), which is difficult for the system to recognize and respond to real-time signals. Nevertheless, the electronic signal characteristics establish a good mapping relationship with the smoking process obtained by optical observation.

3.2.2. Signal of multi-line scanning

Since the upper detector responded faster, it was used to monitor the smoking process in the case of multi-line scanning, as shown in Fig. 10.

In this process, smoking occurred and the electronic signal was captured. As shown in Fig. 10(a), the electron beam began irradiating and the signal stepped up at 0.3 s, attenuated during 0.4–0.5 s, then increased during 0.5–0.6 s. Finally, large peak pulse disturbances appeared during 0.6–1 s

According to analysis in 3.2.1, the pulse disturbances and base value of signals indicated the powder movement behavior. Signal changes in different periods show a corresponding relationship with powder behaviors during different stages, as shown in Fig. 8. The signal

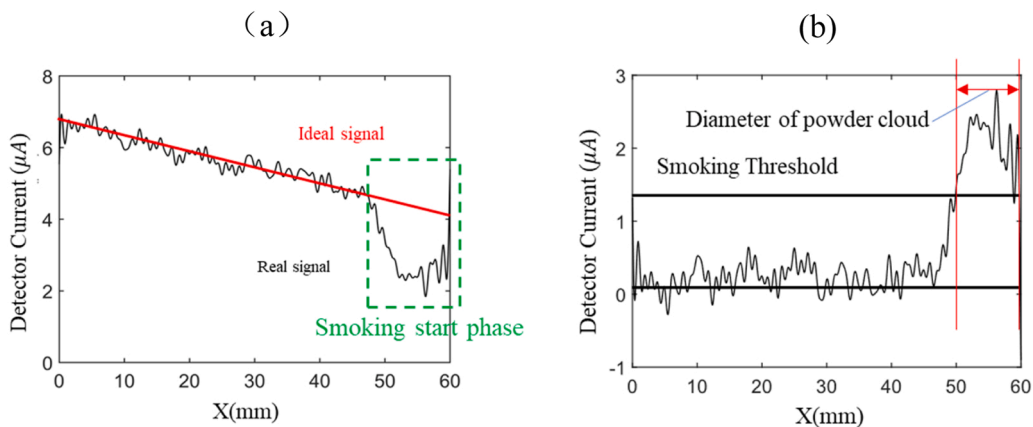


Fig. 11. Recognition method of smoking based on signal attenuation characteristics, (a) comparison between real-time signal and a reference signal, (b) difference value between real-time signal and a reference signal.

attenuation during 0.4–0.5 s demonstrated that a powder cloud appeared and hindered the movement of backscattered electrons and secondary electrons towards the upper detector. At that time, smoking entered the “start-grow stage” before the “explosion stage”, during which local powder clouds appeared above some irradiated areas. Fig. 10(b) shows the waveform of the electronic signal before and after the signal attenuation, in which the signal in the red box is the normal signal before smoking. The signal was presented as a periodic sawtooth wave, and each cycle corresponds to a single scanning line. This was because when the electron beam scanned every single line, the collected electron current decreased as the irradiating position moved away from the detector along the X direction. After 0.36 s, obvious signal attenuation appeared at the end of each scanning line, indicating that the smoking tended to “start” and “grow” at the end of the scan line.

During 0.5–0.6 s, smoking entered the “explosion stage”, the central powder bed appeared and expanded outward and upward. Part of the electrons impacted dispersed powders in the powder cloud and formed backscattered and secondary electrons at this place instead of the powder bed. Thus, more backscattered and secondary electrons reached the detector than “start stage” or “grow stage”, increasing the signal. Meanwhile, with the constant increase of F_q , some powders left the powder bed and moved rapidly outward, finally impacted on the detector after about 0.1 s. This caused the pulses with high peak values in the signal during 0.6–1 s. The peak values are roughly the same as that in the experiment of fixed-position irradiation, indicating that the limit of charge accumulation causing smoking is the same in multiple scanning and fixed-position irradiation.

As Fig. 10 shows, it took about 120 ms from the abnormal signal attenuation to the “explosion stage”, which provides sufficient time for smoking identification and system response. By identifying the attenuation characteristics, smoking can be identified in its early stage, and interrupted by turning off the electron beam in time. As shown in Fig. 11, when the deviation was higher than a certain threshold, it is considered that smoking has started. Fig. 11(a) is the partial enlarged view of the single-cycle curve within the blue frame in Fig. 10(b). The abscissa was converted from time to position coordinate, in order to indicate the real-time distribution of the powder cloud. The red line is the ideal signal, which was fitted out by the signal before smoking. Fig. 11(a) shows the recognition process of the single scan line signal in the blue frame in Fig. 10(b). The red line segment in the figure is the reference signal obtained according to the single scan line signal in the blue frame in the figure. The real-time signal was different from the reference signal. To recognize smoking more intuitively, D-value between the real signal and ideal signal is shown in Fig. 11(b). If D-value exceeds the set threshold, the powder cloud is judged to generate, which indicates that there is a great possibility of smoking.

When the signal deviation exceeds the given threshold for the first time, it indicates that smoking enters the “grow stage” at the end of the corresponding scanning line. Turning off the electron beam at this time can prevent the powder cloud fully from developing, interrupting smoking before the “explosion stage”. By restarting the EB-PBF process at this layer, smoking can be avoided.

Despite that this method based on signal attenuation characteristics recognition requires high data processing speed and needs to establish the reference signal database related to the scanning position in advance. Electronic detection technology provides an effective method for the monitoring and suppression of smoking.

4. Modeling of the smoking phenomenon

Existing studies propose electrostatic force as the main driving force of smoking based on calculations and comparisons of different forces. This explanation reveals the mechanism of powder explosive movement at the early stage of smoking because it considers the accumulation of repelling forces in the static powder bed. However, it may not adapt well to the subsequent stages as powders move to a large distance meanwhile

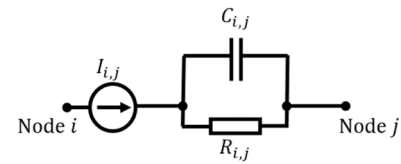


Fig. 12. Resistance-capacitance parallel branch.

the electrostatic force declines. We proposed a numerical model to specifically simulate the characteristic motion behavior of powders that are affected by the electrostatic and inertial forces.

4.1. Model description

4.1.1. Charge dissipation in powder bed

A charge accumulation model was created to depict the charge dissipation process of the powder bed. The model was used to calculate the charge distribution of the powder bed and provide necessary parameters for the subsequent force analysis based on the amount of powder charge. A stationary electron beam with current density obeying Gaussian distribution was used. Considering that some powders overlap in the Z direction on a multilayer powder bed, the current in the electron beam spot was discretized. Then the propagation path of each current was tracked to find the first powder that can be reached, the current was considered to be injected into this powder.

After receiving the current input of the electron beam, electron charge dissipated among the powders and accumulated in them continuously. The charge dissipation in the powder bed is a very complex process, related to both the electrical characteristics and the spatial state of the whole powder bed. In order to realize the simulation of the charge dissipation process in the powder bed, some simplifications were needed. When discussing the charge dissipation process between powder and substrate, Cordero et al. [21] simplified the electrical connection between powder and substrate as a resistance-capacitance parallel circuit. We applied this model and extended the equivalent circuit method to the powder bed in three-dimensional (3D). The whole powder bed can be transformed into a complex 3D resistance capacitance parallel network. To simplify the model and ensure affordable computational cost, the following assumptions were made:

- (1) The electrical connections between powder-powder and powder-substrate were regarded to be the same. The circuit elements on each branch had the same parameters; The current from the upper powder was equally distributed to the lower powders.
- (2) The powder consists of a metal core and an oxide film [29–32]. The connection between every two powders is treated as a parallel branch consisting of a capacitor and an ohmic resistor, as shown in Fig. 13.
- (3) The shortest electron transfer path assumption was applied: the input electrons tended to transfer along the shortest path for minimum dissipation, and reach the substrate through no more than three powders.
- (4) As powders moved, the stacking state of the powder bed changed, meaning the connection states between powders are different at different times. Therefore, the paths of charge transfer need to be redefined at each time step.

According to Assumption(2), the dissipation rate of charge from one powder to another needed to be calculated. We simulated the charge and discharge process of the capacitor under the condition of constant current input, and finally obtained the charge amount of each powder [33], as shown in Fig. 12. For the branch between powders i and j, the circuit equation is:

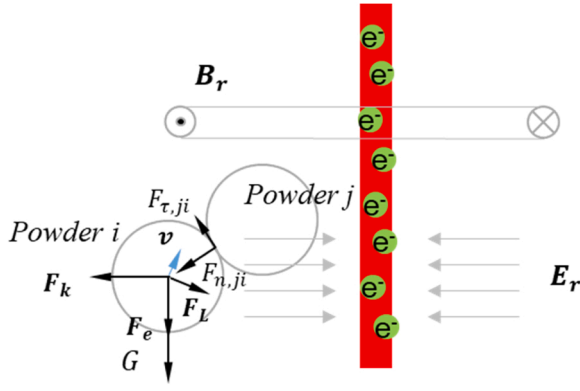


Fig. 13. Force analysis of powders in the smoking process.

$$\frac{dQ_{ij}}{dt} + \frac{Q_{ij}}{\tau} = I_{ij} \quad (1)$$

where Q_{ij} is the charge amount of the capacitor on the branch between powder i and j , representing the amount of charge accumulated because of the poor contact during the current transfer from powder i to j ; $\tau = R_{ij}C_{ij}$ is the charge dissipation time constant, depending on the connection status between two powders[34,35].

By solving Eq. (1), we can obtain:

$$Q_{ij}(t) = I_{ij}\tau + (Q_{ij}(0) - I_{ij}\tau)e^{-t/\tau} \quad (2)$$

where $Q_{ij}(0)$ is the initial amount of charge on the branch i,j .

4.1.2. Powder dynamics

In addition to the gravity and contact forces, the charged powder is also under the action of the electron beam impact force, the magnetic field force, the electric field force, and the electrostatic force, as shown in Fig. 13. The resultant force on the powder can be expressed as [26]:

$$\vec{F}_{total} = \vec{G} + \vec{F}_{contact} + \vec{F}_e + \vec{F}_k + \vec{F}_m + \vec{F}_q \quad (3)$$

The Hertz-Mindlin contact force model employed the contact forces [36–38], including tangential force $\vec{F}_{\tau,ji}$ and normal force $\vec{F}_{n,ji}$, as shown in Fig. 14. The electron beam impact force, electric field force, magnetic field force, and electrostatic force are all involved in the model.

The electron beam impact force (\vec{F}_e) was caused by the momentum transfer between the moving electron and the impacted powder, which can be expressed as

$$F_e = \frac{1}{e}m_e v_e \quad (4)$$

Where F_e is the impact force of an electron beam on powders; e is the charge amount of a single electron; m_e is the mass of a single electron; v_e is the electron velocity, which can be deduced from general relativity. The expression is as follows

$$v_e = c \sqrt{1 - \frac{1}{(1 + \frac{eU}{m_e c^2})^2}} \quad (5)$$

Where c is the light speed under vacuum and U is the acceleration voltage of the electron beam. The electric field force can be expressed as

$$\vec{F}_k = q\vec{E} \quad (6)$$

where q is the charged amount of a powder and the direction of the electric field intensity vector \vec{E} is radial inward. Centered on the axis of the electron beam, the modulus of \vec{E} in 3-D cylindrical coordinates can be expressed as follows

$$E = -\frac{I_0}{2\pi\epsilon_0 v r} (e^{-\frac{\ln 2 r^2}{r_0^2}} - 1) \quad (7)$$

where I_0 is the beam current, ϵ_0 is vacuum permittivity, r_0 is the radius of the beam spot, r is the distance from the space point to the axis, v is the electron velocity. The Lorentz force of moving charged powder can be expressed as

$$\vec{F} = q\vec{v} \times \vec{B} \quad (8)$$

where \vec{v} is the velocity vector of powder movement and q is the charge amount of the powder. \vec{B} is the magnetic induction vector, the modulus can be expressed as

$$B(r) = \frac{\mu_0 I_0}{2\pi r} (1 - \exp(-\frac{\ln 2 r^2}{r_0^2})) \quad (9)$$

where μ_0 is the permeability of the vacuum, I_0 is the beam current, r_0 is the radius of the beam spot, r is the distance from a space point to the axis. The electrostatic force is obtained by solving the system electrostatic energy equation as follows

$$W_e = \frac{1}{2} \sum_n q_k \varphi_k \quad (10)$$

where W_e is the electrostatic energy of the multi-conductor system, q_k is the charge of powder k , φ_k is the potential of powder k . For powder i with charged quantity q , of which the ball center is located at (x,y) , the electrostatic force can be obtained by the virtual work principle[21,39].

Physical constants involved in equations were listed in Table 3.

Table 3
Physical constants involved in equations.

Physical constants	Sign	Value	Unit
Mass of a single electron	m_e	9.10956×10^{-31}	kg
Charge amount of a single electron	e	$1.6021892 \times 10^{-19}$	C
Light speed	c	2.99792458×10^8	m/s
Vacuum permittivity	ϵ_0	$8.854187817 \times 10^{-12}$	F/m
Permeability of vacuum	μ_0	$4\pi \times 10^{-7}$	N/A ²

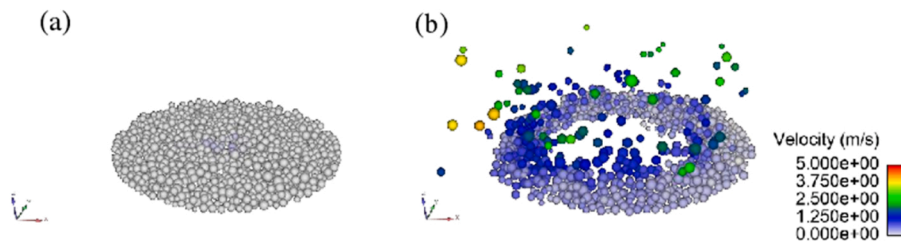


Fig. 14. Situations of powder bed at 500 μ s, (a) neglecting only the electrostatic force, (b) considering electrostatic force.

Table 4
Parameters used in the simulation.

Parameter	Value	Unit	Reference
Accelerate voltage	60	kV	/
Beam spot diameter	200	μm	/
Beam current	2	mA	/
Charge dissipation constant τ	2.86×10^{-6}	s	/
Electron absorptivity η	0.5	/	[41]
Solid density	4.51	g/cm^3	/
Poisson ratio	0.34	/	/
Young's modulus	110	GPa	/
Friction coefficient	0.62	/	[42–45]
Size distribution	45 ~ 105	μm	/

4.2. Simulation implementation

A powder dynamic model was implemented in this study based on the discrete element method taking into account contact stress, friction, gravity, and kinetic equations. In this model, powder particles were regarded as incompressible, inviscid, homogenous, and isotropic, applicable to the Hertz-Mindlin model [40].

The simulation zone was a circular area with a diameter of 2mm. The free-falling model was used to generate a random powder stacking state and finally the initial powder layer of 1000 powder particles [40]. The particle size distribution was 45 ~ 105 μm , obeying the Gaussian distribution of $\sigma = 15\mu\text{m}$. And the average size is 75 μm . The parameters used in the simulation were summarized in Table 4. It should be noted that there is no available data for Ti6Al4V in literature, thus the charge dissipation constant τ measured in the work of Chiba et al. about In718 was used as an approximate [23]. The physical time was about 500 μs . Considering that the electron beam was scattered after it passed through the powder cloud, fewer electrons could reach the simulated zone as smoking developed. Therefore, we use an “equivalent average electron absorptivity” of 0.5, which is less than 0.8 in reference 42. Due to the fact that the performed experiment intentionally omitted the preheating process, the effect of temperature on charge dissipation constant and micro-sintering was neglected in the simulation. Such an arrangement simplifies the simulation complexity without affecting the interpretation of electrostatic and inertial forces in powder motion when smoking is triggered.

Two numerical simulation cases were designed in this section. First was the smoking phenomenon with or without the effect of electrostatic force. The charge dissipation process and powder movement were discussed in this example. Second was the movement of initial static powders after being struck by splashed powders. The splashed powders were set to be charged or uncharged to discuss the mechanism of craters.

5. Discussions on the characteristic mechanisms of smoking

In the above-mentioned analysis, the generation and expansion of the “powder cloud” can be identified by electronic signals, as powder behaviors at a macroscopic scale. However, the specific movement of powders needs to be investigated to reveal the mechanism, which cannot be obtained by macro observation methods.

With the established simulation framework, two groups of comparative cases were obtained: a powder charging model was obtained to verify the accuracy of modeling; a powder impact model was obtained to reveal the mechanism of crater generation and expansion.

5.1. Charging in the start stage of smoking

According to Eqs.(4)-(10), the comparative calculation cases considering different forces were designed, and the results were shown in Fig. 14. Fig. 14(b) shows results that consider all forces, while Fig. 14(a) shows results neglecting F_q . The results proved that F_q was the main

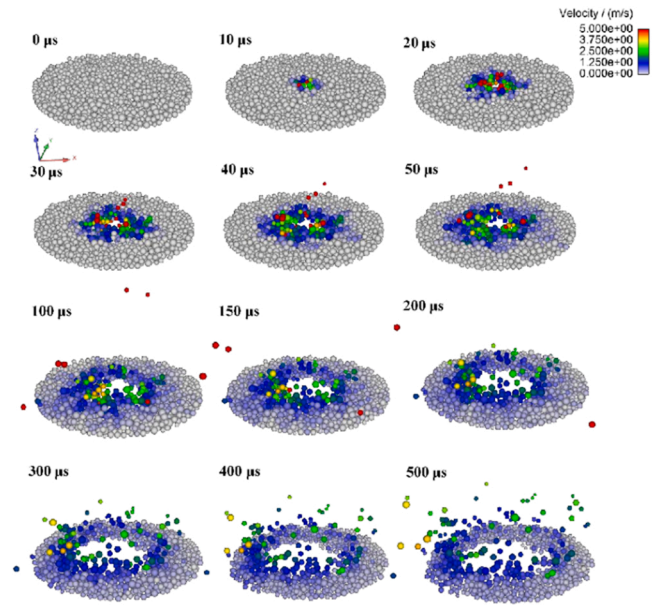


Fig. 15. diagram of powder velocity during smoking under the condition of fixed-position irradiation.

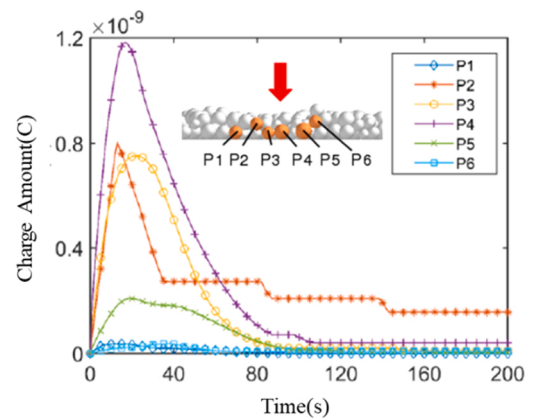


Fig. 16. Charge dissipation curve of target powders.

driving force of smoking.

By calculating different forces of powders at each time step, the maximum value of each force can be obtained: The average gravity of the powder was 10^{-8}N , the maximum electrostatic force was 10^{-3}N , the magnitude of electric field force and impact force was about 10^{-7}N and the magnitude of the magnetic field force was 10^{-14}N . The above results conform to the existing study conclusions on the macro scale: electrostatic force contributes the most to smoking.

Fig. 15 shows the powder velocity distribution of the simulation, reproducing the powder behavior from the “nurture” to the early “grow” stage of smoking. Under the irradiation of the electron beam, there was a small powder disturbance in the irradiated area. After 30 μs , some powders started to push the surrounding powders, then left the powder bed and splashed into the periphery area. Then more powders splashed from the powder bed and kept moving in the upper area, causing a powder cloud. The powder cloud showed a centrosymmetric distribution above the irradiation area. In addition, the speed of splashed powders can reach several meters per second. Apart from the difference in time scale, the above simulation results were in agreement with the optical observation results concerning the stage-wise characteristic.

Fig. 16 shows the charge amount of several selected powders. Each powder showed obvious charging behavior under electron beam

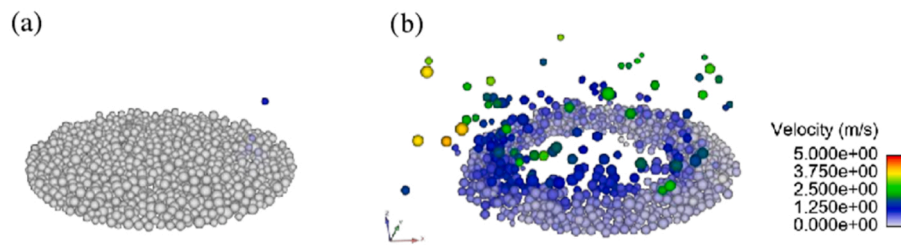


Fig. 17. Powder bed state at 500 μ s under different conditions: (a) 0C, (b) 1×10^{-8} C.

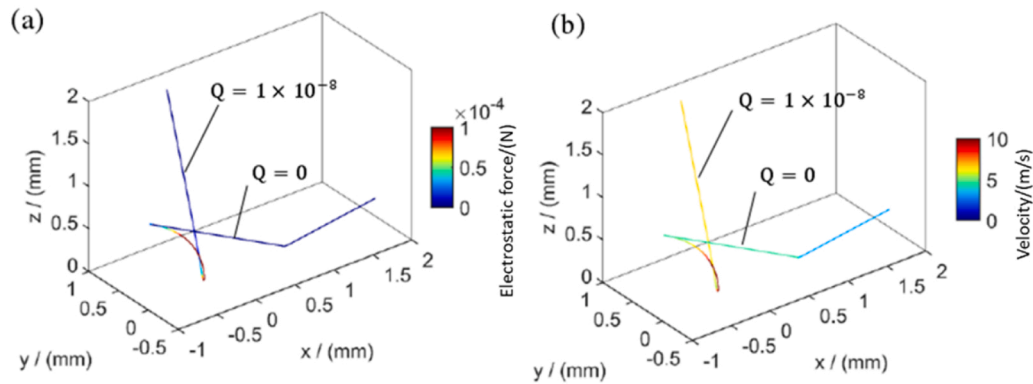


Fig. 18. Evolutions of (a) electrostatic force, and (b) velocity during impact.

irradiation. Among them, P4 splashed outward and might strike the detector finally. P4 powder had the fastest charging speed and reaches the highest charge amount at about 20 μ s. This was because P4 powder is in the center of the irradiated area, where the electron beam current density is the largest.

The charge-discharge processes of other powders were similar, and the farther away from the center of the beam spot, the smaller the maximum charge of the powder. The maximum charge of the powder can reach 1.2×10^{-9} C, which is very close to the value measured based on electronic signals ($\sim 10^{-8}$ C).

5.2. Generation and expansion of craters

Fig. 5 shows the discrete and diffusing “dark spots” observed at the periphery of the irradiated area in the “explosion” stage of smoking. The above model reproduced the movement characteristics of powder in the early “start” and “grow” stages of smoking and revealed its physical mechanism. However, it was simplified to reduce the calculation amount and the calculation domain was small. A new case is proposed in this section to explain the phenomenon of rapid diffusion of smoking in the far field.

According to the optical observation, “dark spots” indicated the existence of local powder disturbance caused by the splashed powder striking the peripheral powder bed, which we called the local powder cloud. Meanwhile, each disturbed area produced new splashed powders to cause a new disturbance, meaning the smoking diffused in a mode similar to the chain reaction. A case was designed in which moving powders moved toward the powder bed at the speed of 5m/s and with different charge amounts. Fig. 17(a) and (b) show the strikes of one uncharged powder and one charged powder on the static powder bed respectively. After being struck by uncharged powder, the powder bed stabilized quickly, while the strike of charged powder caused a violent disturbance.

Fig. 18(a) and (b) are the diagrams of velocity and electrostatic force evolution before and after powder strikes the powder bed. The charged powder was significantly attracted by the electrostatic force from the powder bed, resulting in acceleration and deflection. In this process, the

powder reached a high speed in a very short time and then struck the powder bed. The electrostatic force intensifies the strike of the powder on the powder bed. After the strike process, the speed and electrostatic force of the impacting powder decreased significantly, indicating that it transmitted momentum and charge to the stationary powder. After that, the struck powders splashed and struck the peripheral powder bed in the same way.

The simulation results proved that the strikes caused by charged powder resulted in craters, and verified the conjecture to a certain extent that it promoted the expansion of smoking according to the experimental observation.

6. Conclusions

This study systematically investigates the smoking phenomenon. A high-speed photography system and an electronic signal detection system were built to monitor the smoking phenomenon during the EB-PBF process in real time. Simulation using the discrete element method was conducted to investigate the effect of the inertial force and electrostatic force on the motion of powders. The following conclusions can be drawn:

- (1) Smoking is a sequential process that can be divided into four stages according to the different motion characteristics of the powder bed. The non-uniform spatial distribution of electrons prompts the overcharged powders to splash and strike on the powder bed forming craters and inducing a chain reaction making smoking irreversible.
- (2) Smoking is strongly linked to electron charging and discharging, which is determined by scanning parameters. The generation and vanishing of powder clouds signify it is possible to recover the powder bed before the explosion stage. The interval time between the beam passing the same point may determine whether the powder cloud continues to expand.
- (3) Multistage nature of smoking is confirmed by the strong mapping relationship between measured electronic signals and powder behaviors. The proposed electronic signal monitoring system

shows the potential of recognizing the characteristic signal pattern at the “grow” stage of smoking, providing a new route for predicting and preventing smoking.

- (4) Simulation of powder motion behavior based on charge transfer and powder dynamics model reveals the charging process of powder particles under electron beam irradiation and verifies that the electrostatic force is the main driving force of smoking. The promoting effect of charged particles striking the powder bed on smoking expansion is confirmed.

The current study, investigating the smoking phenomenon from the perspectives of observation, monitoring, and simulation, provided a detailed description of the entire process. Further explorations of specific powder and electron behaviors, including the persistence of powder clouds and the interaction between the electron beam and powders, will be of value.

CRedit authorship contribution statement

Dongfang Wang: Writing – original draft, Visualization, Validation, Methodology, Investigation, Formal analysis, Data curation, Conceptualization. **Dechen Zhao:** Writing – review & editing, Visualization, Validation, Methodology, Investigation, Formal analysis, Data curation, Conceptualization. **Xiaoyu Liang:** Writing – original draft, Visualization. **Xiang Li:** Writing – review & editing. **Feng Lin:** Writing – review & editing, Supervision, Resources, Project administration, Methodology, Funding acquisition, Conceptualization.

Declaration of Competing Interest

The authors declare that they have no known competing financial interests or personal relationships that could have appeared to influence the work reported in this paper.

Data Availability

Data will be made available on request.

Acknowledgment

Authors thank the financial support from the National Natural Science Foundation of China (NSFC) by the NSFC- DFG (Deutsche Forschungsgemeinschaft) Joint Research Program (Grant No. 52061135113).

References

- [1] F. Calignano, et al., Overview on additive manufacturing technologies, *Proc. IEEE* 105 (4) (2017) 593–612.
- [2] L.C. Zhang, et al., Additive manufacturing of titanium alloys by electron beam melting: a review, *Adv. Eng. Mater.* 20 (2018) 5.
- [3] S. Liu, Y.C. Shin, Additive manufacturing of Ti6Al4V alloy: a review, *Mater. Des.* (2019) 164.
- [4] H. Tang, et al., Tantalum bone implants printed by selective electron beam manufacturing (SEBM) and their clinical applications, *Jom* 72 (3) (2020) 1016–1021.
- [5] C. Körner, Additive manufacturing of metallic components by selective electron beam melting - a review, *Int. Mater. Rev.* 61 (5) (2016) 361–377.
- [6] W. Kan, et al., Microstructure and mechanical properties of a high Nb-TiAl alloy fabricated by electron beam melting, *Mater. Des.* 160 (DEC.) (2018) 611–623.
- [7] Y. Li, et al., Microstructure, mechanical properties and strengthening mechanisms of IN738LC alloy produced by Electron Beam Selective Melting, *Addit. Manuf.* (2021) 47.
- [8] Y. Li, et al., Microstructures and mechanical properties evolution of IN939 alloy during electron beam selective melting process, *J. Alloy. Compd.* (2021) 883.
- [9] Larsson, M. and A. Snis, Method and device for producing three-dimensional objects. 2012, Google Patents.
- [10] J. Karlsson, et al., Surface oxidation behavior of Ti–6Al–4V manufactured by Electron Beam Melting (EBM®), *J. Manuf. Process.* 17 (2015) 120–126.
- [11] G. Rizza, M. Galati, L. Iuliano, A phase-field study of neck growth in electron beam powder bed fusion (EB-PBF) process of Ti6Al4V powders under different processing conditions, *Int. J. Adv. Manuf. Technol.* 123 (3) (2022) 855–873.
- [12] NeuBeam. Available from: <https://www.waylandadditive.com/neubeam/>.
- [13] Kitamura, S. and N. Tsutagawa, THREE-DIMENSIONAL LAMINATING AND SHAPING APPARATUS, THREE-DIMENSIONAL LAMINATING AND SHAPING APPARATUS CONTROL METHOD, AND THREE-DIMENSIONAL LAMINATING AND SHAPING APPARATUS CONTROL PROGRAM. 2018.
- [14] U. L., History and Future of EBM, in 1st International Conference on Electron Beam Additive Manufacturing EBAM. 2016: Germany.
- [15] M. Sigl, S.L., M.F. Zaeh. Transient physical effects in electron beam sintering in 17th International Solid Freeform Fabrication Symposium. 2006. Austin, TX, USA.
- [16] C. Eschey, S.L., M.F. Zaeh. Examination of the powder spreading effect in Electron. in 20th International Solid Freeform Fabrication Symposium. 2009. Austin, TX, USA.
- [17] H.B. Qi, et al., Direct metal part forming of 316L stainless steel powder by electron beam selective melting. Proceedings of the Institution of Mechanical Engineers, Part B: Journal of Engineering Manufacture, 2006. 220 (11): p. 1845–1853.
- [18] Kahnert, M., S. Lutzmann, and M.F. Zaeh. Layer formations in electron beam sintering. in 18th International Solid Freeform Fabrication Symposium. 2007. Austin, TX, USA.
- [19] J. Milberg, M. Sigl, Electron beam sintering of metal powder, *Prod. Eng.* 2 (2) (2008) 117–122.
- [20] Zhou, B., Research on Electron Beam and Laser Hybrid Selective Melting System and Process. 2018, Tsinghua University: Beijing, China.
- [21] Z.C. Cordero, et al., Powder bed charging during electron-beam additive manufacturing, *Acta Mater.* 124 (2017) 437–445.
- [22] S. Yim, et al., Ball-milling treatment of gas-atomized Ti 48Al 2Cr 2Nb powder and its effect on preventing smoking during electron beam powder bed fusion building process, *Addit. Manuf.* (2022) 51.
- [23] A. Chiba, et al., Smoke suppression in electron beam melting of inconel 718 alloy powder based on insulator-metal transition of surface oxide film by mechanical stimulation, *Materials* (16) (2021) 14.
- [24] J. Schwerdtfeger, R.F. Singer, C. Körner, In situ flaw detection by IR-imaging during electron beam melting. *Rapid Prototyp. J.* 18 (4) (2012) 259–263.
- [25] Sigl, M., S. Lutzmann, and M.F. Zaeh, Transient Physical Effects in Electron Beam Sintering, in International Solid Freeform Fabrication Symposium. 2006.
- [26] Eschey, C., S. Lutzmann, and M. Zaeh. Examination of the powder spreading effect in electron beam melting (EBM). in 2009 International Solid Freeform Fabrication Symposium. 2009. University of Texas at Austin.
- [27] D.C. Zhao, F. Lin, Dual-detector electronic monitoring of electron beam selective melting, *J. Mater. Process. Technol.* (2021) 289.
- [28] S. Yim, et al., Effect of mechanical ball milling on the electrical and powder bed properties of gas-atomized Ti–48Al–2Cr–2Nb and elucidation of the smoke mechanism in the powder bed fusion electron beam melting process, *J. Mater. Sci. Technol.* 137 (2023) 36–55.
- [29] M. Owen, XPS study of the initial growth of oxide films on Inconel 600 alloy, *Appl. Surf. Sci.* 2 (1) (1978) 55–73.
- [30] M.D.C. Belo, N. Hakiki, M. Ferreira, Semiconducting properties of passive films formed on nickel–base alloys type Alloy 600: influence of the alloying elements, *Electrochim. Acta* 44 (14) (1999) 2473–2481.
- [31] G. Lorang, et al., AES depth profiling of passive overlayers formed on nickel alloys, *Surf. Interface Anal.* 16 (1–12) (1990) 325–330.
- [32] G. Lewis, X-ray photoelectron study of surface layers on orthopaedic alloys. I. Ti–6Al–4V (ASTM F6) alloy, *J. Vac. Sci. Technol. A Vac. Surf. Films* 11 (2) (1993) 325–335.
- [33] M. Zahn, *Electromagnetic Field Theory: a problem solving approach*, Wiley, 1979.
- [34] A.R. Von Hippel, S. Morgan, Dielectric materials and applications, *J. Electrochem. Soc.* 102 (3) (1955) 68Ca.
- [35] W.D. Kingery, H.K. Bowen, D.R. Uhlmann, *Introduction to Ceramics*, Vol. 17, John Wiley & Sons, 1976.
- [36] A. Di Renzo, F.P. Di Maio, Comparison of contact-force models for the simulation of collisions in DEM-based granular flow codes, *Chem. Eng. Sci.* 59 (3) (2004) 525–541.
- [37] C. Thornton, S.J. Cummins, P.W. Cleary, An investigation of the comparative behaviour of alternative contact force models during inelastic collisions, *Powder Technol.* 233 (2013) 30–46.
- [38] Y. Tsuji, T. Tanaka, T. Ishida, Lagrangian numerical simulation of plug flow of cohesionless particles in a horizontal pipe - ScienceDirect, *Powder Technol.* 71 (3) (1992) 239–250.
- [39] Banerjee, S. and M. Levy, Approximate capacitance expressions for two equal sized conducting spheres, in Proc. ESA Annu. Meet. Electrostatics. 2014.
- [40] Chen Hui, et al., Powder-spreading mechanisms in powder-bed-based additive manufacturing: experiments and computational modeling, *Acta Mater.* 179 (2019) 158–171.
- [41] Yan Wentao, et al., Multiscale modeling of electron beam and substrate interaction: a new heat source model, *Comput. Mech.* 56 (2) (2015) 265–276.
- [42] B. Alchikh-Sulaiman, F. Ein-Mozaffari, A. Lohi, Evaluation of poly-disperse solid particles mixing in a slant cone mixer using discrete element method, *Chem. Eng. Res. Des.* 96 (2015) 196–213.
- [43] Paul W. Cleary, A multiscale method for including fine particle effects in DEM models of grinding mills, *Miner. Eng.* 84 (2015) 88–99.
- [44] K.F. Lee, et al., Development of a multi-compartment population balance model for high-shear wet granulation with discrete element method, *Comput. Chem. Eng.* 99 (apr.6) (2017) 171–184.
- [45] Chen Hui, et al., Flow behavior of powder particles in layering process of selective laser melting: numerical modeling and experimental verification based on discrete element method, *Int. J. Mach. Tools Manuf.* 123 (2017) 146–159.